

# Multi-Cation Synergistic Confinement Enables Long-Cycling Ultrahigh-Nickel Cathodes

Yichao Cui, Xudong Zhang,\* Yanan Xu, Shani Li, Gefei Zhang, Xiong Zhang, Xianzhong Sun, Kai Wang,\* and Yanwei Ma\*

The growing demand for high-specific-energy batteries has driven significant interest in ultrahigh-nickel-layered oxide cathodes. However, rapid structural degradation during cycling remains a critical barrier to their large-scale commercialization. Herein, a multi-cation synergistic confinement strategy to enhance the structural stability of ultrahigh-nickel  $\text{LiNi}_{0.9}\text{Co}_{0.06}\text{Mn}_{0.04}\text{O}_2$  (NCM90) cathodes is reported. Zr, Mg, and Al are robust gradient-diffused into the NCM90 lattice during *in situ* synthesis, leveraging the strong Zr—O and Al—O bonding energies to mitigate lattice distortion. Additionally, the pillar effect of  $\text{Mg}^{2+}$  in the Li layer helps preserve structural integrity during

charge/discharge cycles. Meanwhile,  $\text{Zr}^{4+}$  segregates on the surface of the NCM90 lattice, forming a  $\text{Li}_x\text{Zr}_y\text{O}_z$  coating that effectively alleviates interfacial side reactions. As a result, the Zr/Mg/Al-co-doped NCM90 (NCM-ZMA) achieves a superior capacity retention of 94.2% after 200 cycles at 1 C (2.8–4.3 V), significantly outperforming the pristine NCM90 (82.5%). This work demonstrates that a rational doping strategy, integrating both crystal structure design and interface engineering, can maximize the long-term cyclability of ultrahigh-nickel cathodes, paving the way for their widespread application in high-energy battery systems.

## 1. Introduction

The rapid development of new energy industries, such as portable electronics and electric vehicles, has driven the increasing demand for lithium-ion batteries (LIBs) with high-energy density and long cycle life.<sup>[1,2]</sup> Among the cathode candidates for LIBs, high-nickel ternary cathode materials ( $\text{LiNi}_x\text{Co}_y\text{Mn}_{1-x-y}\text{O}_2$ ,  $x \geq 0.6$ ) are considered one of the most promising options due to their high discharge-specific capacity ( $>200 \text{ mAh g}^{-1}$ ), high operating voltage, and relatively low cost.<sup>[3–5]</sup> To further pursue higher energy density, increasing the nickel content in NCM cathodes has emerged as an effective strategy. Ultrahigh-nickel ternary cathodes ( $\text{LiNi}_x\text{Co}_y\text{Mn}_{1-x-y}\text{O}_2$ ,  $x \geq 0.9$ ) are particularly notable, delivering reversible capacities exceeding  $220 \text{ mAh g}^{-1}$  at a cutoff voltage of 4.3 V, while also reducing raw material costs.

However, the increased nickel content in ultrahigh-nickel ternary cathodes leads to severe cycling instability during

charge/discharge processes.<sup>[6]</sup> This instability primarily stems from phase transitions in ternary-layered oxides, evolving from the original hexagonal phase (H1) to a monoclinic phase (M), followed by another hexagonal phase (H2), and finally to a third hexagonal phase (H3).<sup>[7]</sup> Among these, the H2–H3 phase transition poses significant threats to structural integrity.<sup>[8]</sup> During this transition, the lattice undergoes anisotropic contraction along the c axis, generating substantial lattice strain. Repeated phase transitions induce localized stress accumulation, initiating and propagating microcracks within particles, ultimately leading to pulverization.<sup>[9]</sup> Moreover, these microcracks facilitate electrolyte penetration into the particles, triggering intensified side reactions that exacerbate cathode degradation and reduce  $\text{Li}^{+}$  diffusion coefficients.<sup>[10]</sup> Furthermore, under deep lithium extraction conditions, irreversible oxygen evolution reactions, irreversible phase transitions, and transition metal (TM) dissolution occur, collectively contributing to a progressive decline in battery performance.<sup>[11–13]</sup>

To address the aforementioned challenges, researchers have employed various strategies to improve the performance of high-nickel ternary cathode materials for LIBs. Among these, bulk doping and surface/interface engineering have emerged as the most widely adopted modification approaches.<sup>[14–16]</sup> A variety of dopants have been proposed, including  $\text{Mo}^{6+}$ ,<sup>[17]</sup>  $\text{B}^{3+}$ ,<sup>[18]</sup>  $\text{Zr}^{4+}$ ,<sup>[18,19]</sup>  $\text{Al}^{3+}$ ,<sup>[20]</sup>  $\text{Sn}^{4+}$ ,<sup>[21]</sup>  $\text{Mg}^{2+}$ ,<sup>[22,23]</sup> and  $\text{Nb}^{5+}$ .<sup>[24]</sup> For instance, Yang-Kook Sun et al.<sup>[25]</sup> utilized Al/Nb co-doping to enhance the crystal structure and optimize primary particle morphology, achieving a capacity retention rate of 88.3% after 1000 cycles in full-cell configurations. Surface modification techniques, such as surface coating and surface-layer structure design, have also been explored. For example, Feng Pan et al.<sup>[26]</sup> developed a high-entropy rock-salt phase surface layer through Zr/Al co-doping, which not only improved lithium-ion diffusion kinetics but also

Y. Cui, X. Zhang, Y. Xu, S. Li, G. Zhang, X. Zhang, X. Sun, K. Wang, Y. Ma  
Institute of Electrical Engineering  
Chinese Academy of Sciences  
Beijing 100190, P. R. China  
E-mail: xdzhang@mail.iee.ac.cn  
wangkai@mail.iee.ac.cn  
ywma@mail.iee.ac.cn

Y. Cui, X. Zhang, Y. Xu, S. Li, G. Zhang, X. Zhang, X. Sun, K. Wang, Y. Ma  
School of Engineering Sciences  
University of Chinese Academy of Sciences  
Beijing 100049, P. R. China

Y. Ma  
School of Materials Science and Engineering  
Zhengzhou University  
Zhengzhou 450001, P. R. China

 Supporting information for this article is available on the WWW under <https://doi.org/10.1002/batt.202500244>

suppressed interface side reactions and surface structural degradation. In a half-cell configuration, this approach achieved a capacity retention rate of 74.9% after 500 cycles at 1 C. Furthermore, Yongming Zhu et al.<sup>[27]</sup> implemented a dual-modification strategy involving bulk engineering and surface reconstruction to optimize high-nickel cathode materials. By utilizing different sources of Nb for Nb doping and Li<sub>3</sub>PO<sub>4</sub> coating, they achieved a capacity retention rate of 91.38% after 200 cycles at 1 C in a half-cell configuration. These studies demonstrate the potential of combined approaches to enhance the electrochemical performance of high-nickel ternary cathodes.

The roles of different dopants in high-nickel ternary cathode materials have been extensively investigated. Among these, Al<sup>3+</sup> has been widely applied due to its ability to stabilize the

host-layered structure, enhance resistance to microcracks, and thus improve the cyclic life of the cathode material.<sup>[19]</sup> Additionally, Al<sup>3+</sup> effectively suppresses Li–Ni cation mixing, thereby enhancing the rate performance of the material.<sup>[28]</sup> Mg<sup>2+</sup> exhibits distinct behavior as a dopant element, predominantly occupying Li sites.<sup>[29]</sup> During deep Li extraction, Mg<sup>2+</sup> acts as a structural pillar, effectively inhibiting the irreversible H<sub>2</sub>–H<sub>3</sub> phase transition and significantly improving the cyclic stability of the material.<sup>[30]</sup> Furthermore, Zr<sup>4+</sup> has been identified as a promising dopant for surface modification. When incorporated, Zr<sup>4+</sup> tends to segregate on the surface of cathode material particles, forming a Li–Zr–O compound.<sup>[19,31]</sup> This surface layer not only provides excellent protection against harmful electrolyte attacks but also maintains high-Li<sup>+</sup>-ionic

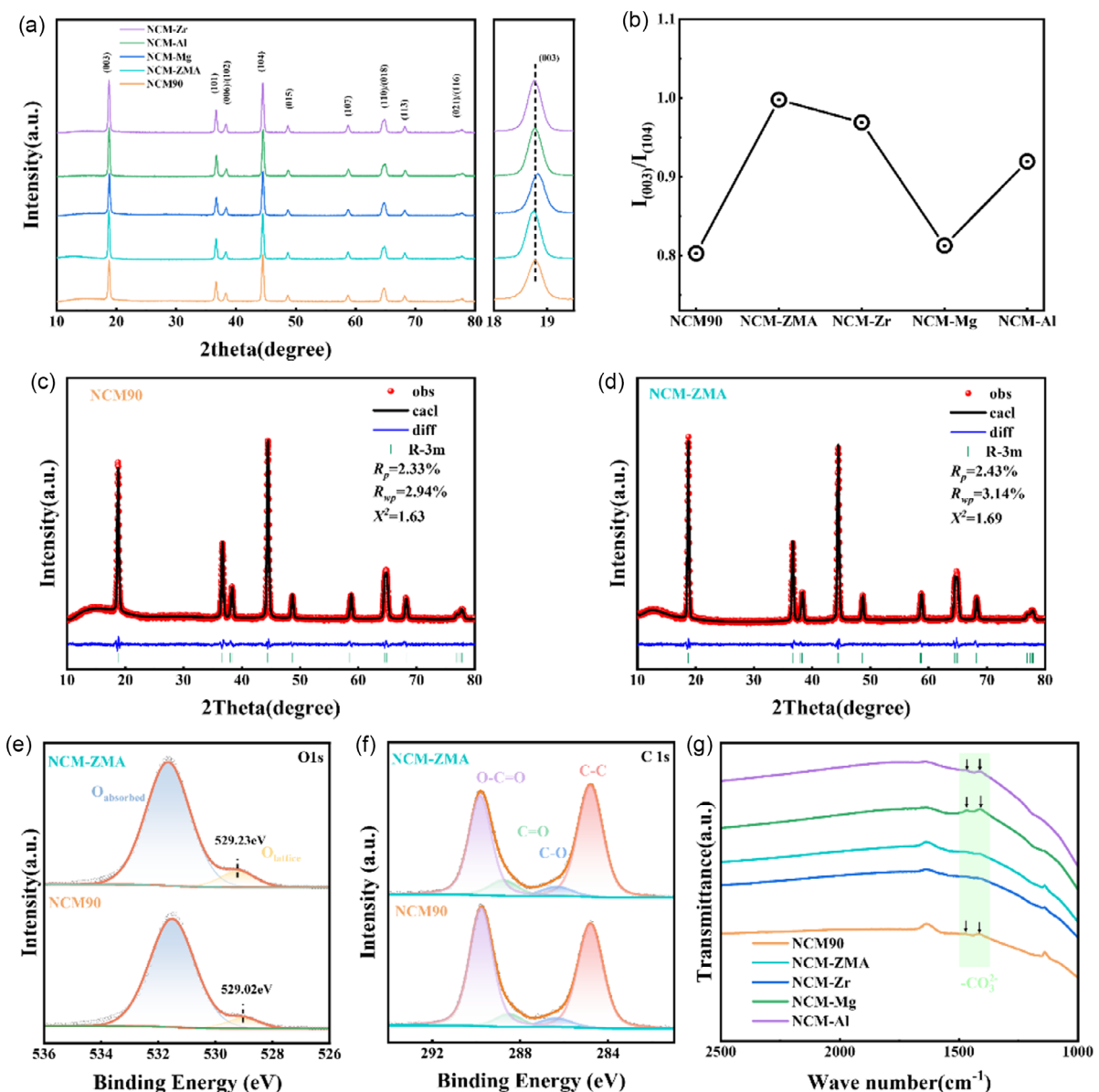


**Figure 1.** a) XRD patterns with magnified views of (003) peaks; b) the I(003)/I(104) of NCM90, NCM-ZMA, NCM-Zr, NCM-Mg, and NCM-Al; Rietveld refinements of XRD patterns for c) NCM90 and d) NCM-ZMA; XPS patterns of e) O 1s and f) C 1s; and g) FTIR spectra of NCM90, NCM-ZMA, NCM-Zr, NCM-Mg, and NCM-Al.

conductivity, thereby preserving the integrity of the material's surface.<sup>[18,26,32,33]</sup>

Inspired by these findings, this study employs Zr/Mg/Al co-doping to modify the ultrahigh-nickel cathode  $\text{LiNi}_{0.9}\text{Co}_{0.06}\text{Mn}_{0.04}\text{O}_2$  (NCM90), leveraging the synergistic effects of these dopants to enhance structural and interfacial stability. Comprehensive characterization reveals that Zr/Mg/Al co-doping effectively suppresses Li/Ni cation mixing, mitigates irreversible phase transitions, optimizes surface chemistry by reducing residual lithium species, enhances  $\text{Li}^+$  transport, and inhibits interfacial side reactions. The modified Zr–Mg–Al co-doped high-entropy NCM90 (NCM–ZMA) cathode delivers an initial discharge capacity of 207  $\text{mAh g}^{-1}$  (0.1 C, 2.8–4.3 V) and retains 94.2% of its capacity after 200 cycles at 1 C, demonstrating superior cycling performance.

## 2. Results and Discussion

The NCM–ZMA, its single-element-doped counterparts (NCM–Zr, NCM–Mg, NCM–Al), and pristine NCM90 were synthesized through lithiation-assisted sintering. X-ray diffraction (XRD) analysis systematically elucidated the structural modulation mechanisms of dopants in the layered crystal framework. As shown in Figure 1a, all samples display characteristic diffraction peaks corresponding to the hexagonal  $\alpha\text{-NaFeO}_2$ -type structure (space group R-3m) without detectable impurity phases, confirming the preservation of intrinsic-layered framework integrity during

doping. Comparative analysis reveals distinct lattice parameter variations across different doped systems. Specifically, the (003) diffraction peak of NCM–Zr exhibits a low-angle shift, signifying c-axis expansion. This phenomenon stems from the substitution of  $\text{Ni}^{3+}$  (0.56 Å) and  $\text{Ni}^{2+}$  (0.69 Å) by larger  $\text{Zr}^{4+}$  ions (0.72 Å) in TM layers, causing lattice expansion.<sup>[34]</sup> In contrast, NCM–Mg shows a high-angle shift at the (003) peak, indicating c-axis contraction. This contraction arises from  $\text{Mg}^{2+}$  (0.72 Å) preferentially occupying  $\text{Li}^+$  sites (0.76 Å), thereby reducing lithium layer interplanar spacing.<sup>[35,36]</sup> For NCM–Al, negligible (003) peak shift indicates minimal lattice distortion from  $\text{Al}^{3+}$  (0.535 Å) incorporation, while its strong covalent bonding with oxygen atoms effectively stabilizes the crystalline framework. The degree of cationic disorder in NCM90 and doped samples was determined using the intensity ratio of the (003) to (104) diffraction peaks,  $I(003)/I(104)$ , as shown in Figure 1b. Compared to the pristine NCM9, the ratios for NCM–Zr and NCM–Al exhibit significant increases, confirming the efficacy of Zr/Al doping in suppressing  $\text{Li}^+/\text{Ni}^{2+}$  cation mixing.<sup>[37]</sup> In contrast, NCM–Mg shows a comparable ratio to the undoped material, indicating that  $\text{Mg}^{2+}$ , primarily occupying  $\text{Li}$  sites, has minimal impact on cationic ordering.<sup>[38]</sup> Strikingly, the co-doped NCM–ZMA achieves the highest  $I(003)/I(104)$  ratio, demonstrating the synergistic role of Zr, Mg, and Al in enhancing structural order and cationic stability.

Rietveld refinement was performed on the XRD patterns of NCM–ZMA and NCM90 to quantify their structural parameters (Figure 1c,d). As summarized in Table S2, Supporting Information, co-doping induces an increase in lattice constants from

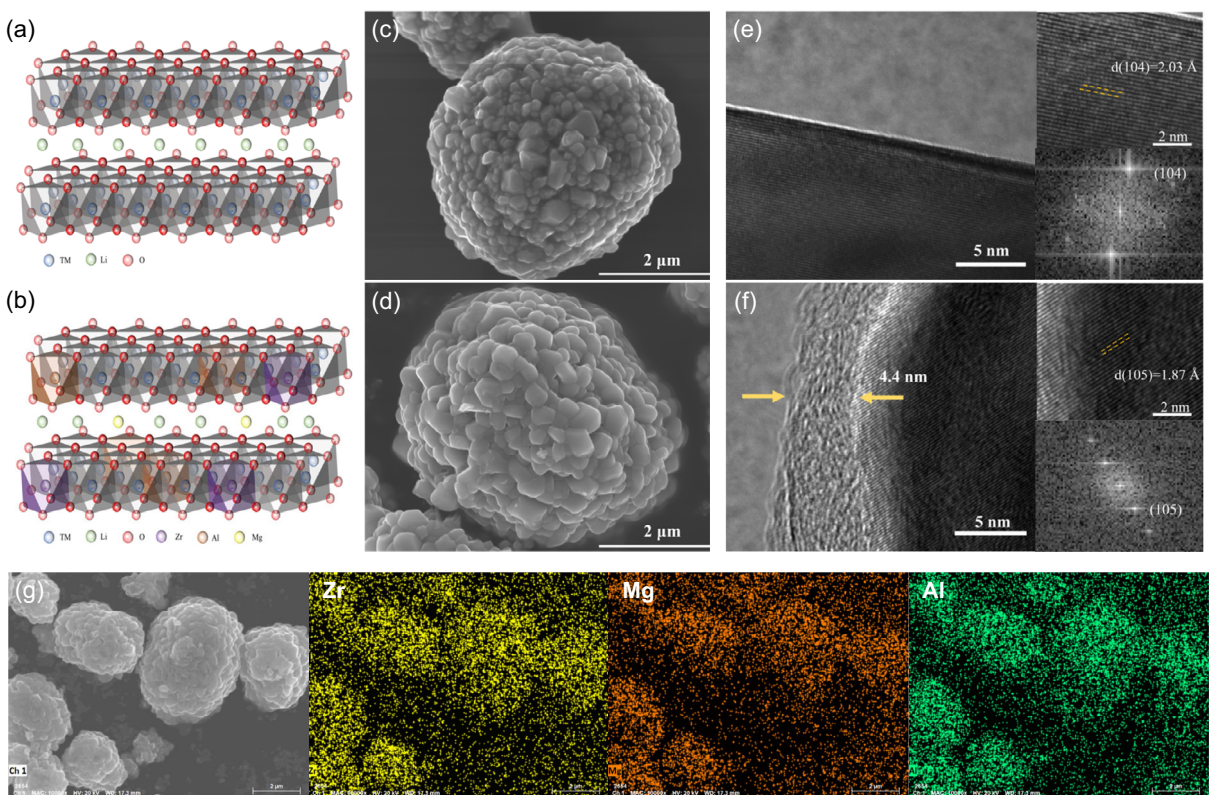


**Figure 2.** Structural configurations of a) NCM90 and b) NCM–ZMA; SEM images of c) NCM90 and d) NCM–ZMA; e) HRTEM images and FFT images of NCM90 and f) NCM–ZMA; and g) EDS elemental mapping of Zr, Mg, and Al elements.

$a = 2.8728 \text{ \AA}$  and  $c = 14.1825 \text{ \AA}$  for NCM90 to  $a = 2.8729 \text{ \AA}$  and  $c = 14.1864 \text{ \AA}$  in NCM-ZMA. The expanded interlayer spacing facilitates improved  $\text{Li}^+$  diffusion kinetics. Critically, Li/Ni mixing degree decreases from 2.9% in NCM90 to 1.27% in NCM-ZMA. This improvement can be attributed to the synergistic effect that the pinning effect exerted by  $\text{Zr}^{4+}$  and  $\text{Al}^{3+}$  ions within the TM layers effectively inhibits  $\text{Ni}^{2+}$  migration into Li layers.<sup>[39]</sup> These structural enhancements collectively endow NCM-ZMA with superior  $\text{Li}^+$  transport kinetics and structural stability, providing a foundation for enhanced electrochemical performance.<sup>[40,41]</sup>

The surface chemical environment of the material was systematically characterized via X-ray photoelectron spectroscopy (XPS) and Fourier-transform infrared spectroscopy (FTIR). For the O 1s XPS spectra (Figure 1e), a significant increase in the intensity of the lattice oxygen ( $\text{O}^{2-}$ , 529.23 eV) peak was observed in NCM-ZMA compared to NCM90, coupled with a positive shift in binding energy by 0.21 eV. This enhancement stems from

the strong covalent interaction between oxygen and high-electronegativity dopants ( $\text{Zr}^{4+}$ ,  $\text{Al}^{3+}$ ), which form robust TM–O bonds (TM = Zr, Al) with increased bond energies, thereby suppressing lattice oxygen evolution. C 1s XPS analysis (Figure 1f) further revealed that the intensity of the characteristic lithium carbonate ( $\text{OCO}_2$ , 289.8 eV) peak was significantly reduced in NCM-ZMA, confirming effective mitigation of surface residual lithium species. This observation was corroborated by the FTIR spectra (Figure 1g). While NCM90 displays distinct  $\text{CO}_3^{2-}$  vibration bands at 1433 and 1490  $\text{cm}^{-1}$ , these peaks are absent in NCM-ZMA and NCM-Zr.<sup>[42]</sup> Consistent with prior studies,  $\text{Zr}^{4+}$  doping facilitates surface Li–Zr–O compound formation (e.g.,  $\text{Li}_2\text{ZrO}_3$ ), which scavenges free  $\text{Li}^+$  ions and inhibits  $\text{Li}_2\text{CO}_3$  generation.

The structural configurations of NCM90 and NCM-ZMA are schematically depicted in Figure 2a,b, respectively. Scanning electron microscopy (SEM) images (Figure 2c,d) demonstrate that both materials display spherical secondary particles with a

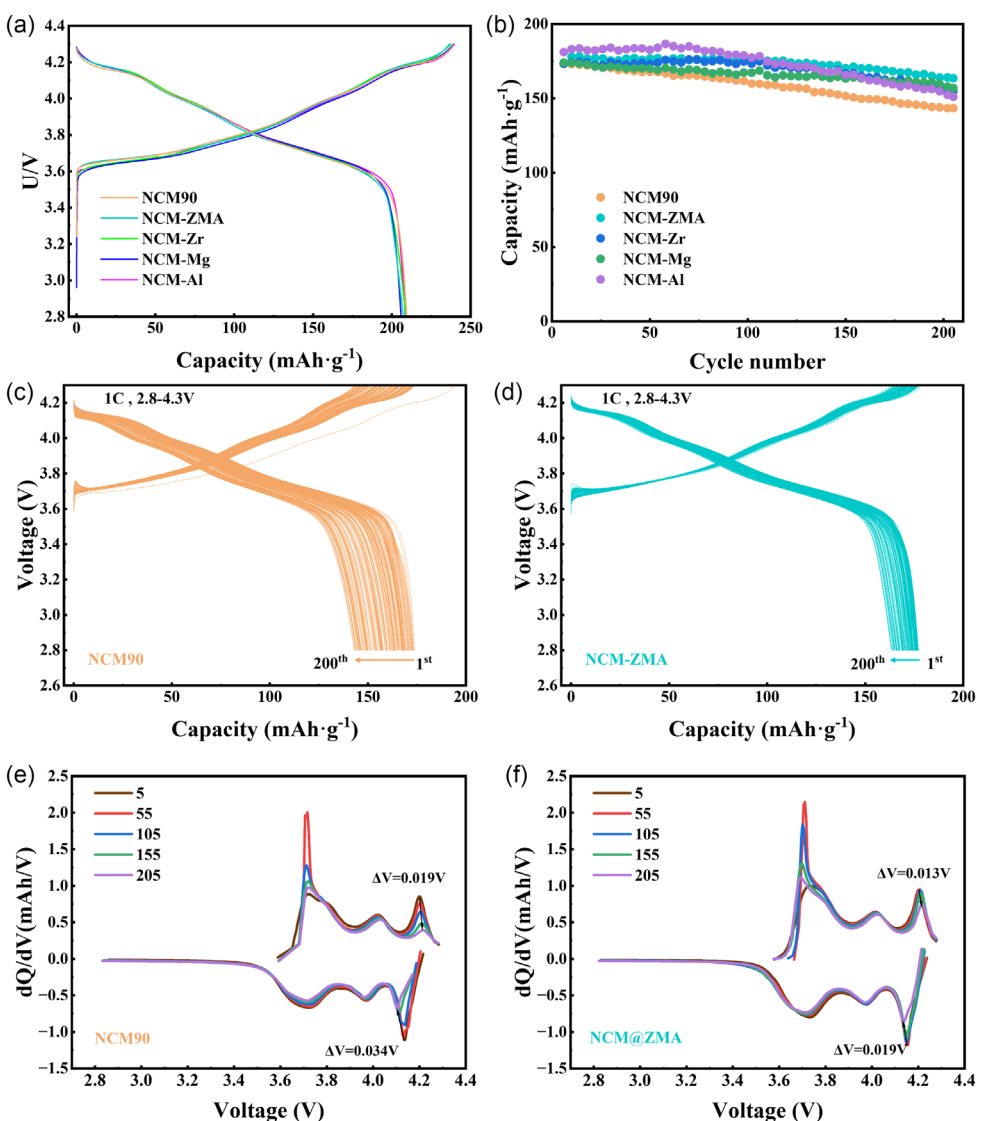


**Figure 3.** a) Initial charge–discharge curves at 0.1 C and b) the cycling performance at 1 C of NCM90, NCM-ZMA, NCM-Zr, NCM-Mg, and NCM-Al conducted at 25 °C in the range of 2.8–4.3 V; charge–discharge profiles in c) half-cells NCM90 and d) NCM-ZMA within 2.8–4.3 V at 1 C and 25 °C; and the  $dQ/dV$  profiles of e) the NCM90 and f) NCM-ZMA.

uniform size distribution centered at  $\approx 5 \mu\text{m}$ . Notably, NCM-ZMA retains a well-defined micron-scale spheroidal architecture composed of nanoscale primary particles, closely resembling the morphological characteristics of pristine NCM90. High-resolution transmission electron microscopy (HRTEM) and fast Fourier transform (FFT) analyses (Figure 2e,f) demonstrate that both materials maintain well-ordered layered structures. Strikingly, a 4.4 nm thick amorphous coating is detected on NCM-ZMA particles, while absent on NCM90. XPS analysis (Figure S1 and Table S1, Supporting Information) reveals an increased proportion of  $\text{Ni}^{2+}$  in the near-surface region of NCM-ZMA due to charge compensation effects induced by the surface enrichment of  $\text{Zr}^{4+}$ , which demonstrates the coating layer may be composed of  $\text{Li}_x\text{Zr}_y\text{O}_z$ . This structural and interfacial synergy, combining expanded interlayer spacing and surface passivation, critically enhances the electrochemical properties by simultaneously facilitating  $\text{Li}^+$  diffusion and suppressing electrolyte decomposition.<sup>[43]</sup>

Energy-dispersive X-ray spectroscopy (EDS) elemental mapping confirms the homogeneous distribution of Zr, Mg, and Al throughout the NCM-ZMA sample (Figure 2g and Figure S2, Supporting Information), validating successful multi-cation doping.

The electrochemical performance of NCM90, NCM-ZMA, and single-element-doped counterparts (NCM-Zr, NCM-Mg, NCM-Al) was evaluated in CR2032 coin-type half-cells with a voltage window of 2.8–4.3 V. Initial charge–discharge profiles at 0.1 C (Figure 3a) show negligible differences among the cathodes. Specifically, the first-cycle discharge capacities of NCM-ZMA and NCM90 are 207.2 and 209.4  $\text{mAh g}^{-1}$ , respectively.

Cycling stability tests at 1 C (Figure 3b) reveal markedly improved capacity retention for NCM-ZMA (94.2%) compared to NCM90 (82.5%) after 200 cycles. The single doped samples exhibit intermediate capacity retention values of 89.3, 90.1, and 83.4% for NCM-Zr, NCM-Mg, and NCM-Al, respectively. The charge–discharge curves of NCM90 and NCM-ZMA after

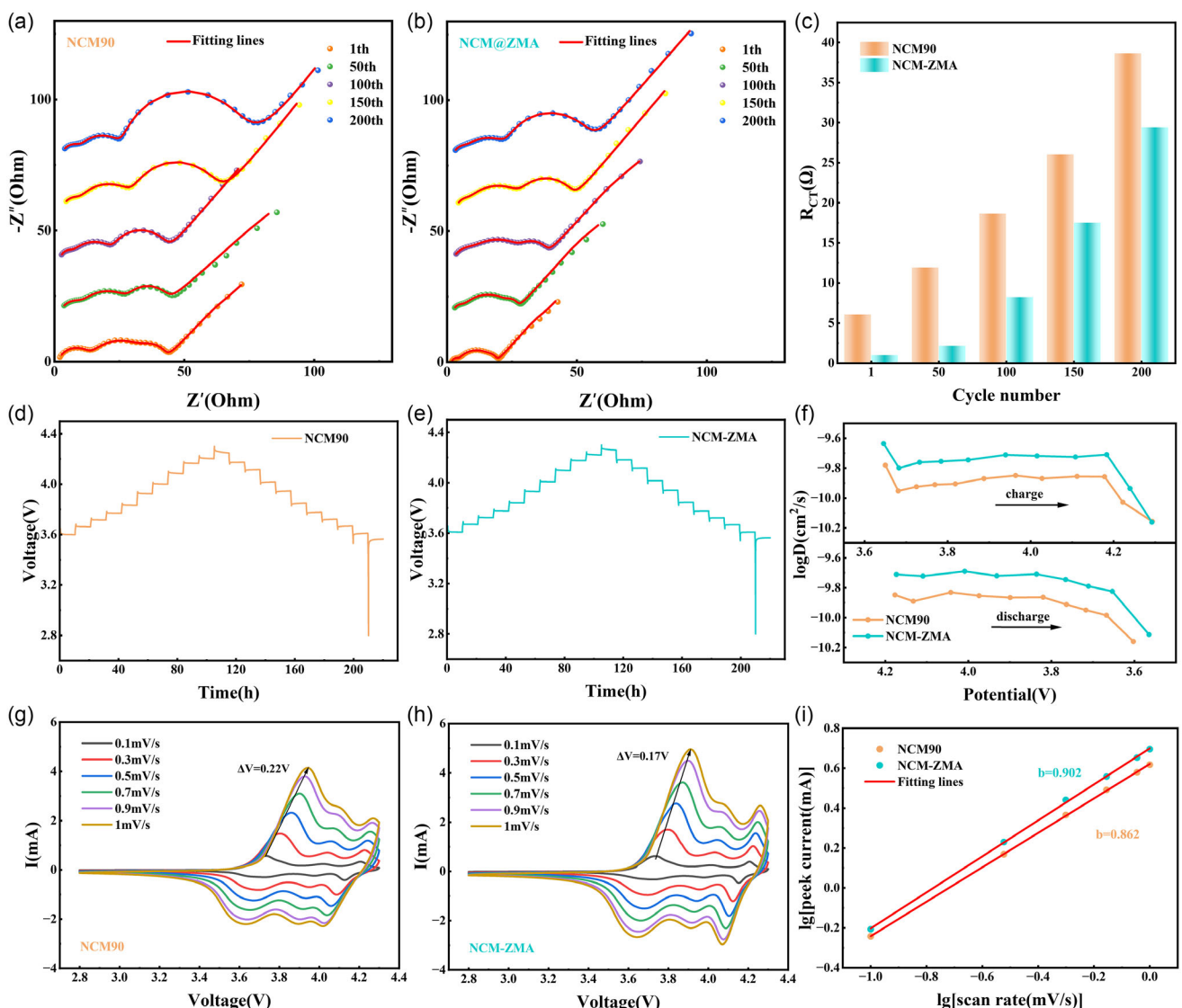


**Figure 4.** Nyquist plots and fitting lines upon various cycles of a) NCM90 and b) NCM-ZMA; c)  $R_{\text{ct}}$  values obtained from EIS fitting; GITT curves of d) NCM90 and e) NCM-ZMA; f) GITT profiles obtained during charge and discharge process of NCM90 and NCM-ZMA; CV profiles of g) NCM90 and h) NCM-ZMA at different scan rates between 2.8 and 4.3 V; and i) linear relationship between maximum peak current of charge and logarithm of scan rate.

200 cycles at a 1 C rate, as depicted in Figure 3c,d, reveal that NCM-ZMA maintains both high capacity and a stable discharge voltage during cycling. In contrast, the discharge voltage attenuation becomes increasingly severe for NCM90 with additional cycles, indicating a relatively faster increase in polarization and greater resistance accumulation during cycling.<sup>[27]</sup>

The differential capacity ( $dQ/dV$ ) curves of NCM90 and NCM-ZMA (Figure 3e,f) demonstrate that, with an increase in the number of cycles, the intensity of the H2–H3 phase transformation peaks in NCM90 significantly weakens. After 300 cycles, the peak shift reaches 0.019 V during charging and 0.034 V during discharging, which are higher than the corresponding values of 0.013 and 0.019 V observed in NCM-ZMA. This indicates a marked deterioration in phase transformation reversibility and a progressively severe structural collapse. In stark contrast, NCM-ZMA exhibits only a slight reduction in the intensity of the H2–H3 phase transformation peaks and minimal peak shifting, confirming stable phase transition reversibility and structural integrity.<sup>[19]</sup>

As shown in Figure S3, the cyclic performance of the five cathode materials was evaluated at a 0.5 C rate. After 150 cycles, the capacity retention rates for NCM-ZMA, NCM-Zr, NCM-Mg, NCM-Al, and NCM90 are 96.6, 88.5, 92.9, 87.7, and 87.3%, respectively. NCM-ZMA continues to exhibit an excellent capacity retention rate. Additionally, NCM-Mg demonstrates good cyclic performance at both 0.5 C and 1 C rates, which is due to the Mg<sup>2+</sup> ion doping sites being predominantly located in the Li layer, which creates a pillar effect.<sup>[23]</sup> This inhibits the occurrence of irreversible phase transformations during deep Li extraction. However, NCM-Mg performs less satisfactorily in terms of capacity, as Mg<sup>2+</sup> occupies Li<sup>+</sup> sites, thereby reducing the available locations for reversible Li<sup>+</sup> ion deintercalation and intercalation. NCM-Zr and NCM-Al demonstrate improvements not only in cyclic performance but also in capacity. This is because Zr<sup>4+</sup> and Al<sup>3+</sup> primarily occupy doping sites in the TM layers, where they strengthen the structural stability through the formation of strong Zr–O and Al–O bonds.<sup>[19]</sup> Additionally, they effectively prevent the migration of Ni<sup>2+</sup> into the Li layer, thereby reducing the Li/Ni mixing index and ensuring that more sites in the Li layer remain available for reversible Li<sup>+</sup> ion deintercalation and intercalation. The synergistic interplay of Zr, Mg, and Al endows NCM-ZMA with the best comprehensive performance.

The interfacial impedance evolution of NCM90 and NCM-ZMA half-cells was systematically investigated via electrochemical impedance spectroscopy (EIS) at a constant voltage of 4.0 V (vs. Li<sup>+</sup>/Li) (Figure 4a,b). The impedance data were interpreted using an equivalent circuit model (Figure S4, Supporting Information), where the high-, mid-, and low-frequency semicircles correspond to the solid-electrolyte interphase resistance ( $R_1$ ) on the Li anode, the cathode surface passivation layer resistance ( $R_2$ ) and charge-transfer resistance ( $R_{ct}$ ) associated with the cathode, respectively.<sup>[28,44]</sup> As shown in Figure 4c,  $R_{ct}$  for NCM90 remains consistently higher than that of NCM-ZMA throughout cycling, highlighting superior Li<sup>+</sup> migration kinetics and reduced interfacial polarization in the co-doped material. After 200 cycles,  $R_{ct}$  increases from 6.09 to 38.66 Ω for NCM90, whereas for NCM-ZMA, it rises from 1.00 to 29.44 Ω. This attenuated impedance growth in NCM-ZMA is attributed to its Li–Zr–O passivation

layer, which simultaneously enhances Li<sup>+</sup> conductivity and suppresses electrolyte decomposition.<sup>[27,31]</sup> Lithium-ion diffusion coefficients ( $D_{Li^+}$ ) were quantified via galvanostatic intermittent titration technique (GITT) (Figure 4d–f). The co-doped NCM-ZMA exhibits significantly enhanced  $D_{Li^+}$  values compared to NCM90, validating bulk structure optimization via Zr/Mg/Al doping. This enhancement stems from a reduced Li<sup>+</sup> migration energy barrier and accelerated ion transport kinetics.<sup>[45]</sup> Cyclic voltammetry (CV) experiments (Figure 4g,h) are performed to assess the electrochemical performance at varying scan rates (0.1–1.0 mV s<sup>-1</sup>). The CV curves reveal more symmetric redox peaks for NCM-ZMA across all scan rates and the H1–M phase transition peak shifts by 0.17 V, which is lower than the 0.22 V shift observed in NCM90, indicative of enhanced electrochemical reversibility and reduced polarization. Linear fitting of peak current ( $i_p$ ) versus scan rate ( $v$ ) relationship ( $i_p = av^b$ ) is performed in Figure 4i. The results demonstrate an increase in the  $b$ -value from 0.862 for NCM90 to 0.902 for NCM-ZMA, suggesting increased capacitive contribution and diminished diffusion limitations.<sup>[46]</sup>

The kinetic superiority of NCM-ZMA originates from the synergistic interplay between attenuated interfacial resistance and accelerated bulk Li<sup>+</sup> transport. This multi-scale optimization synergistically enhances electrochemical performance, manifested

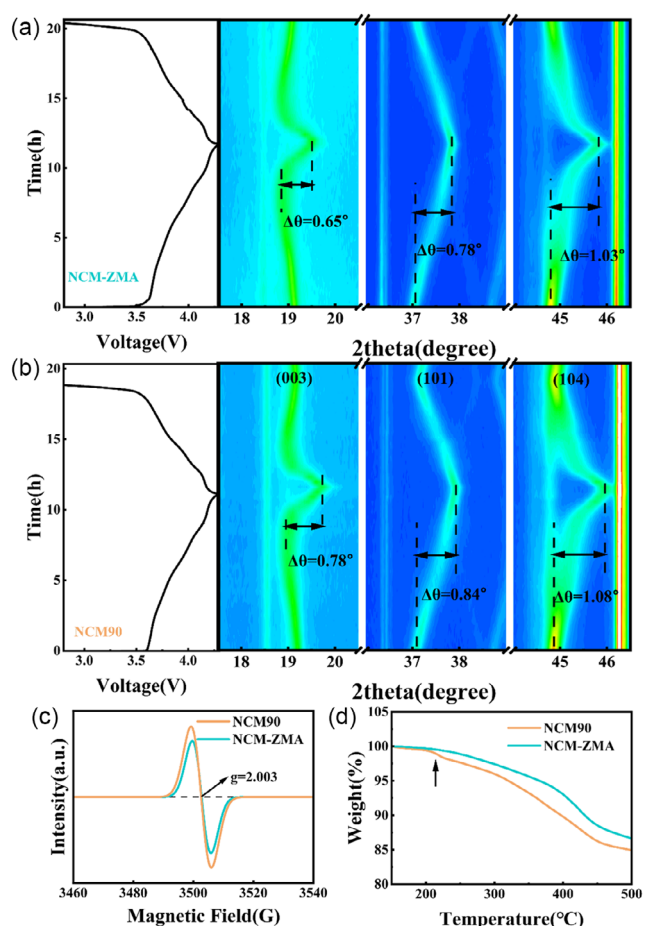


**Figure 5.** In situ XRD characterization for a) NCM-ZMA and b) pristine NCM90 cathodes during the first cycle within 2.8–4.3 V; c) EPR spectra and d) TGA profiles of NCM-ZMA and NCM90.

through higher-Li<sup>+</sup> diffusivity, reduced CV peak separation, and lower charge-transfer resistance.

The structural evolution of NCM-ZMA and NCM90 during the first charge–discharge cycle (0.1 C, 2.8–4.3 V) was monitored via *in situ* XRD analyses (Figure 5a,b). As the charging voltage increases from 2.8 to 4.1 V, the H1–M–H2 phase transition occurs, accompanied by a low-angle shift of the (003) peaks for both samples, indicating *c*-axis expansion.<sup>[45]</sup> This expansion arises from enhanced interlayer Coulombic repulsion due to Li<sup>+</sup> extraction. Upon further charging to 4.3 V, triggering the H2–H3 phase transition, the (003) peaks shift rapidly to higher angles, signifying rapid *c*-axis contraction.<sup>[47]</sup> Notably, the (003) peak shift magnitude of NCM-ZMA ( $\Delta 2\theta = 0.65^\circ$ ) is significantly smaller than that of NCM90 ( $\Delta 2\theta = 0.78^\circ$ ), demonstrating mitigated *c*-axis contraction. This suppression is attributed to two mechanism that 1) the

pillar effect of Mg<sup>2+</sup> in Li slabs, which inhibits TM layer slippage and 2) the lattice anchoring effect of Zr<sup>4+</sup>/Al<sup>3+</sup>, where robust TM–O bonds buffer phase transition stress and minimize lattice distortion. Concurrently, the shifts in the (101) and (104) peaks of NCM-ZMA ( $\Delta 2\theta = 0.78^\circ$ ,  $\Delta 2\theta = 1.03^\circ$ ) are significantly smaller than those of NCM90 ( $\Delta 2\theta = 0.84^\circ$ ,  $\Delta 2\theta = 1.08^\circ$ ), confirming that multi-cation doping alleviates lattice distortion induced by Ni<sup>3+</sup> oxidation. The enhanced lattice oxygen stability is further investigated using electron paramagnetic resonance (EPR) and thermogravimetric analysis (TGA). EPR spectra of NCM-ZMA and NCM90 powder particles (Figure 5c) reveal that NCM-ZMA exhibits a lower oxygen vacancy signal intensity ( $g = 2.003$ ) compared to NCM90, indicating reduced oxygen vacancy formation due to high-entropy doping.<sup>[48]</sup> TGA profiles of charged NCM-ZMA and NCM90 (Figure 5d) demonstrate thermal distinct behaviors that

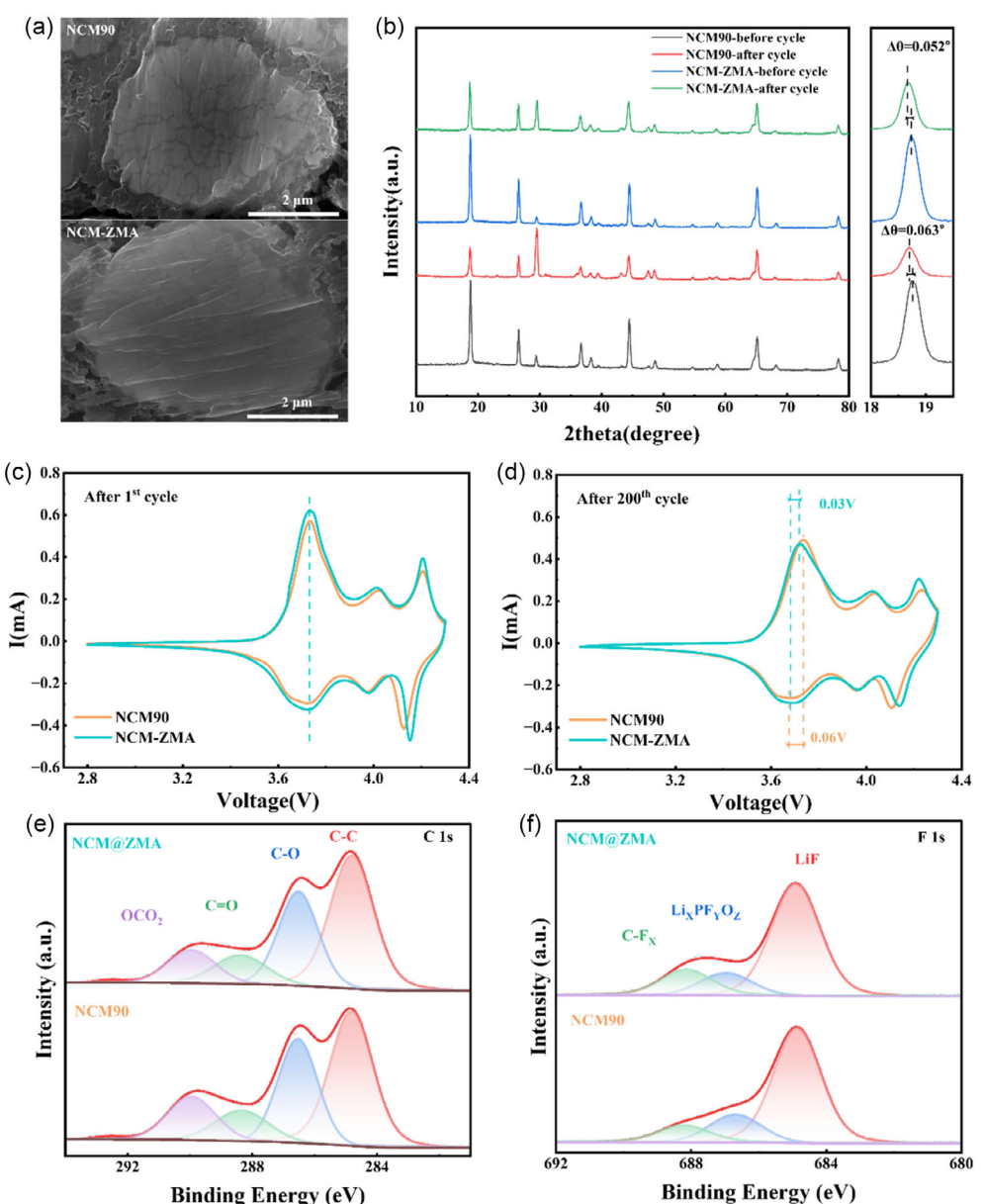


**Figure 6.** a) SEM images for NCM90 and NCM-ZMA; b) XRD patterns and magnified view of the (003) peak; CV profiles of NCM90 and NCM-ZMA after c) 1st cycle and d) 200th cycle with a scan rate of  $0.1 \text{ mV s}^{-1}$ ; e) C 1s and f) F 1s spectrum after 200 cycles at 1 C.

NCM90 experiences significant mass loss at  $\approx 220$  °C, due to lattice oxygen release, while NCM-ZMA exhibits only gradual mass reduction as the temperature increases. NCM90 exhibits a mass loss of 2.35% at 250 °C, whereas NCM-ZMA demonstrates significantly reduced mass loss of 1.12%.<sup>[27]</sup> This confirms that high-entropy doping enhances lattice oxygen stability, suppressing oxygen evolution and mitigating structural degradation during cycling, thereby improving long-term cyclability.<sup>[15,49]</sup>

Cross-sectional SEM images of NCM90 and NCM-ZMA electrodes after 200 cycles at 1 C are presented in Figure 6a. Pronounced through-cracks propagate within NCM90 secondary particles, whereas NCM-ZMA exhibits only minor surface micro-cracks, demonstrating superior mechanical stability of the co-doped material. This striking contrast originates from suppressed irreversible H<sub>2</sub>-H<sub>3</sub> phase transitions in NCM-ZMA, which effectively inhibit intergranular crack initiation and propagation.<sup>[50]</sup> XRD patterns pre- and post-cycling (Figure 6b) reveal that the (003) peak shift in cycled NCM-ZMA is smaller than that of NCM9, confirming doping-induced mitigation of lattice strain during volume contraction/expansion. The CV curves of NCM90 and NCM-ZMA after the first cycle and 100th cycle reveals the superior electrochemical reversibility of NCM-ZMA as indicated by the retention of the original redox peaks. Electrochemical polarization during charge-discharge processes was quantified by the potential difference ( $\Delta E$ ) between the redox peaks. As shown in Figure 6c, negligible differences in  $\Delta E$  were observed among the two cathodes after the first cycle. However, after 200 cycles (Figure 6d), the  $\Delta E$  of NCM90 increased significantly more than that of NCM-ZMA, demonstrating its enhanced stability against polarization during prolonged cycling.<sup>[27]</sup> XPS analysis of the electrode surfaces after 200 cycles at 1 C is conducted to evaluate interfacial evolution. In the C 1s spectra (Figure 6e), the C-C component originates from conductive additives and binders, while the C=O, C=O, and OCO<sub>2</sub> signals are associated with ROCO<sub>2</sub>Li ( $R$  = alkyl), ROLi, and Li<sub>2</sub>CO<sub>3</sub>, indicative of electrolyte decomposition.<sup>[45]</sup> C=O, C=O, and OCO<sub>2</sub> intensity in NCM-ZMA is lower than that in NCM90. Moreover, the F 1s spectra (Figure 6f) reveal significantly lower intensity of Li<sub>x</sub>PF<sub>y</sub>O<sub>z</sub>-related peaks in NCM-ZMA compared to pristine NCM90.<sup>[45]</sup> These suggest suppressed electrolyte decomposition and reduced accumulation of side products on the surface of co-doped materials. Additionally, the comparable C-F<sub>x</sub> peak intensities in both samples indicate the formation of cathode-electrolyte interphase layers is more stable in NCM-ZMA.<sup>[51]</sup> Collectively, these results confirm that high-entropy doping simultaneously enhances structural integrity and optimizes interfacial stability, rationalizing the exceptional cycling performance of NCM-ZMA.

### 3. Conclusion

In this study, a multi-cation co-doping strategy is introduced to enhance the structural stability of NCM90-layered oxide cathodes. During synthesis, Zr, Mg, and Al are systematically introduced into the NCM90 lattice. Zr and Al preferentially occupy TM layers, forming robust Zr-O and Al-O bonds with significantly higher bonding energies than TM-O (TM = Ni, Co, Mn) bonds. This

enhances lattice anchoring and suppresses Ni cation disorder. Meanwhile, Mg predominantly occupies Li slabs, where Mg<sup>2+</sup> acts as a structural pillar to inhibit lattice distortion under deep Li extraction. The synergistic effects of these dopants work collectively to improve the structural robustness of the cathode. Additionally, Zr<sup>4+</sup> reacts with residual Li<sup>+</sup> during synthesis to form a Li<sub>2</sub>Zr<sub>y</sub>O<sub>z</sub> coating, which mitigates interfacial side reactions while enhancing Li<sup>+</sup> transport kinetics. As a result, the co-doped NCM-ZMA achieves a high discharge capacity of 207 mAhg<sup>-1</sup> (0.1 C, 2.8–4.3 V) and a remarkable capacity retention of 94.2% after 200 cycles at a 1 C rate (2.8–4.3 V), significantly outperforming the 82.5% retention of pristine NCM90. This study demonstrates that the multi-cation co-doping strategy effectively stabilizes ultrahigh-nickel cathodes, providing valuable insights for the structural design of high-performance LIB cathodes.

### 4. Experimental Section

#### Material Synthesis

The pristine NCM90 powder was synthesized via a two-step solid-state reaction. TM hydroxide precursor (Ni<sub>0.9</sub>Co<sub>0.06</sub>Mn<sub>0.04</sub>(OH)<sub>2</sub>) and LiOH (molar ratio TM:Li = 1:1.02) were homogenized by milling, followed by calcination under flowing O<sub>2</sub> (450 °C for 5 h and 725 °C for 10 h).

For Zr/Mg/Al-co-doped NCM (NCM-ZMA), a wet-chemical premixing method was employed. At first, TM hydroxide precursor, 0.75 at% ZrO(NO<sub>3</sub>)<sub>2</sub>·xH<sub>2</sub>O, 0.75 at% C<sub>2</sub>H<sub>4</sub>MgO<sub>6</sub>, and 0.25 at% Al(NO<sub>3</sub>)<sub>3</sub>·9H<sub>2</sub>O were added to a solution mixed with 5:1 volume ration of ethanol and deionized water. And the mixture was stirred continuously at 70 °C until dryness, and then vacuum-dried at 80 °C for 12 h. Finally, the doped precursor was mixed with LiOH (TM:Li = 1:1.04), and then sintered under identical O<sub>2</sub> conditions as NCM90. Single-element-doped analogs (NCM-Zr, NCM-Mg, NCM-Al) were prepared following the same protocol with 1 mol% dopant concentration for each element.

#### Analytical Techniques

The crystal structures of the samples were characterized by XRD (Bruker D8, Cu Ka radiation) which was recorded in the 2θ range of 10°–80° with a scan rate of 5° min<sup>-1</sup>. Rietveld refinement was subsequently performed using GASA-2 software. Morphological analyses were conducted via SEM (Hitachi S-4800) and HRTEM (JEOL JEM-F200, FEI Tecnai G2 F30). Elemental distribution mapping was performed by EDS coupled to the SEM. Surface chemistry characterization included XPS (Thermo Scientific ESCALAB 250Xi) and FTIR (Thermo Fisher Scientific Nicolet iS20). Thermal stability was assessed by TGA under argon flow (50 mL min<sup>-1</sup>), heating from 30 to 500 °C at 5 °C min<sup>-1</sup>. Oxygen vacancy concentrations were quantified via EPR (Bruker EMXplus-6/1) spectroscopy.

#### Electrochemical Measurement

Electrochemical evaluations were performed using CR2032 coin-type half-cells assembled in an argon-filled glove box (H<sub>2</sub>O < 0.1 ppm, O<sub>2</sub> < 0.1 ppm) at ambient temperature. First, 80 wt% active material, 10 wt% polyvinylidene fluoride binder, and 10 wt% Super C45 conductive carbon were homogenized in N-methyl-2-pyrrolidone solvent, which was then coated onto aluminum foil followed by vacuum-drying at 100 °C for ≥ 8 h in a vacuum oven. Dried electrodes were cut into 11 mm discs with active material mass loading of 2.0–

3.0 mg cm<sup>-2</sup>. Coin cells were assembled with a polypropylene monolayer separator and lithium metal for the counter electrode. The electrolyte was 1.2 M LiPF<sub>6</sub> in mixture of ethylene carbonate: diethyl carbonate : dimethyl carbonate (EC:DEC:DMC = 1:1:1 by volume ratio) with 1 wt% vinylene carbonate. Electrochemical characterization was conducted via galvanostatic cycling at 2.8–4.3 V versus Li<sup>+</sup>/Li using Neware system at a series of current densities (1 C = 200 mA g<sup>-1</sup>), CV at 0.1–1.0 mV s<sup>-1</sup> scan rates and 2.8–4.3 V range, GITT, and EIS at a frequency range from 0.01 Hz to 200 KHz.

## Acknowledgements

This work was supported by the Beijing Natural Science Foundation of China (grant no. Z230018), the National Natural Science Foundation of China (grant nos. 52207250 and 52377218), and Institute of Electrical Engineering, CAS (grant no. E155110101).

## Conflict of Interest

The authors declare no conflict of interest.

## Author Contributions

**Yichao Cui:** conceptualization (equal); data curation (lead); formal analysis (lead); investigation (equal); writing—original draft (lead); writing—review & editing (equal). **Xudong Zhang:** data curation (equal); formal analysis (equal); funding acquisition (equal); investigation (equal); writing—original draft (equal); writing—review & editing (equal). **Yanan Xu:** data curation (equal); formal analysis (equal). **Shani Li:** data curation (equal); investigation (equal). **Gefei Zhang:** data curation (equal); formal analysis (equal). **Xiong Zhang:** funding acquisition (equal); investigation (equal). **Xianzhong Sun:** formal analysis (equal); investigation (equal). **Kai Wang:** conceptualization (equal); data curation (equal); formal analysis (equal); funding acquisition (equal); project administration (equal); supervision (equal); writing—review & editing (lead). **Yanwei Ma:** conceptualization (equal); funding acquisition (equal); project administration (equal); supervision (equal); writing—review & editing (equal).

## Data Availability Statement

The data that support the findings of this study are available from the corresponding author upon reasonable request.

**Keywords:** high-entropy dopings · LiNi<sub>0.9</sub>Co<sub>0.06</sub>Mn<sub>0.04</sub>O<sub>2</sub> (NCM90) · long-cyclings · synergistic confinements · ultrahigh-nickel cathodes

- [1] M. L. Mao, X. Ji, Q. Y. Wang, Z. J. Lin, M. Y. Li, T. Liu, C. L. Wang, Y. S. Hu, H. Li, X. J. Huang, L. Q. Chen, L. M. Suo, *Nat. Commun.* **2023**, *14*, 13.
- [2] J. Liu, Z. J. Du, X. L. Wang, S. Tan, X. Y. Wu, L. X. Geng, B. H. Song, P. H. Chien, S. M. Everett, E. Y. Hu, *Energy Environ. Sci.* **2021**, *14*, 6441.
- [3] Y. D. Jiang, F. Q. R. Guo, L. Qiu, T. L. Liu, Y. Hu, W. Yang, Y. Liu, Y. Sun, Z. G. Wu, Y. Song, X. D. Guo, *ACS Appl. Mater. Interfaces* **2023**, *15*, 35072.

- [4] W. D. Li, A. Dolocan, P. Oh, H. Celio, S. Park, J. Cho, A. Manthiram, *Nat. Commun.* **2017**, *8*, 10.
- [5] M. Bianchini, M. Roca-Ayats, P. Hartmann, T. Brezesinski, J. Janek, *Angew. Chem.-Int. Edit.* **2019**, *58*, 10434.
- [6] X. Q. Zeng, C. Zhan, J. Lu, K. Amine, *Chem* **2018**, *4*, 690.
- [7] M. Jiang, D. L. Danilov, R. A. Eichel, P. H. L. Notten, *Adv. Energy Mater.* **2021**, *11*, 44.
- [8] Q. Y. Lin, W. H. Guan, J. Meng, W. Huang, X. Wei, Y. W. Zeng, J. X. Li, Z. Zhang, *Nano Energy* **2018**, *54*, 313.
- [9] J. Kim, H. Lee, H. Cha, M. Yoon, M. Park, J. Cho, *Adv. Energy Mater.* **2018**, *8*, 25.
- [10] H. Liu, M. Wolf, K. Karki, Y. S. Yu, E. A. Stach, J. Cabana, K. W. Chapman, P. J. Chupas, *Nano Lett.* **2017**, *17*, 3452.
- [11] K. J. Park, H. G. Jung, L. Y. Kuo, P. Kaghazchi, C. S. Yoon, Y. K. Sun, *Adv. Energy Mater.* **2018**, *8*, 9.
- [12] H. H. Sun, A. Manthiram, *Chem. Mat.* **2017**, *29*, 8486.
- [13] G. W. Nam, N. Y. Park, K. J. Park, J. Yang, J. Liu, C. S. Yoon, Y. K. Sun, *ACS Energy Lett.* **2019**, *4*, 2995.
- [14] T. Weigel, F. Schipper, E. M. Erickson, F. A. Susai, B. Markovsky, D. Aurbach, *ACS Energy Lett.* **2019**, *4*, 508.
- [15] J. S. Xu, J. H. You, Y. S. Wu, R. G. Zheng, H. Y. Sun, Y. G. Liu, S. Liu, Z. Y. Wang, *J. Colloid Interface Sci.* **2025**, *682*, 961.
- [16] X. Liu, K. Yang, L. Zhang, W. Wang, S. Zhou, B. Wu, M. Xiong, S. Yang, R. Tan, *Energy Mater. Adv.* **2024**, *5*, 0131.
- [17] L. Qiao, Q. You, X. Y. Wu, H. H. Min, X. M. Liu, H. Yang, *ACS Appl. Mater. Interfaces* **2024**, *16*, 4772.
- [18] C. H. Li, X. D. Zhang, Y. C. Cui, Y. N. Xu, X. Zhang, X. Z. Sun, K. Wang, Y. W. Ma, *Batteries Supercaps* **2024**, *7*, 9.
- [19] X. Ou, T. C. Liu, W. T. Zhong, X. M. Fan, X. Y. Guo, X. J. Huang, L. Cao, J. H. Hu, B. Zhang, Y. S. Chu, G. R. Hu, Z. Lin, M. Dahbi, J. Alami, K. Amine, C. H. Yang, J. Lu, *Nat. Commun.* **2022**, *13*, 12.
- [20] H. H. Sun, G. R. Pastel, S. S. Zhang, D. T. Tran, J. L. Allen, *J. Electrochem. Soc.* **2022**, *169*, 8.
- [21] T. T. Nguyen, U. H. Kim, C. S. Yoon, Y. K. Sun, *Chem. Eng. J.* **2021**, *405*, 8.
- [22] J. L. Wang, Y. Nie, C. Miao, Y. Tan, M. Y. Wen, W. Xiao, *J. Colloid Interface Sci.* **2021**, *601*, 853.
- [23] S. W. Woo, S. T. Myung, H. Bang, D. W. Kim, Y. K. Sun, *Electrochim. Acta* **2009**, *54*, 3851.
- [24] M. H. Chu, Z. Y. Huang, T. E. Zhang, R. Wang, T. L. Shao, C. Q. Wang, W. M. Zhu, L. H. He, J. Chen, W. G. Zhao, Y. G. Xiao, *ACS Appl. Mater. Interfaces* **2021**, *13*, 19950.
- [25] S. B. Lee, N. Y. Park, G. T. Park, U. H. Kim, S. J. Sohn, M. S. Kang, R. M. Ribas, R. S. Monteiro, Y. K. Sun, *ACS Energy Lett.* **2024**, *9*, 740.
- [26] Z. X. Xu, X. H. Chen, W. G. Fan, M. Z. Zhan, X. L. Mu, H. B. Cao, X. H. Wang, H. Y. Xue, Z. H. Gao, Y. Z. Liang, J. J. Liu, X. H. Tan, F. Pan, *ACS Nano* **2024**, *18*, 33706.
- [27] Z. Li, H. Yi, X. D. Li, P. Gao, Y. M. Zhu, *ACS Appl. Mater. Interfaces* **2024**, *16*, 28537.
- [28] Z. H. Cui, Z. Z. Guo, A. Manthiram, *Adv. Energy Mater.* **2023**, *13*, 15.
- [29] Z. L. Tan, X. X. Chen, J. Lin, Y. D. Huang, W. H. Cheng, Q. C. Liu, H. Zhang, F. C. Ren, Y. D. Huang, Z. J. Liu, T. Brezesinski, Y. Yang, W. G. Zhao, *Angew. Chem.-Int. Edit.* **2025**, *64*, 12.
- [30] H. Darjazi, E. Gonzalo, B. Acebedo, R. Cid, M. Zarzabeitia, F. Bonilla, M. A. Muñoz-Márquez, F. Nobili, *Mater. Today Sustainability* **2022**, *20*, 9.
- [31] Y. V. Baklanova, I. Y. Arapova, A. L. Buzlukov, A. P. Gerashenko, S. V. Verkhovskii, K. N. Mikhalev, T. A. Denisova, I. R. Shein, L. G. Maksimova, *J. Solid State Chem.* **2013**, *208*, 43.
- [32] W. Tang, N. Shen, X. Xiong, H. Liu, X. Sun, J. Guo, F. Jiang, T. Wang, Y. Ma, Y. Zhong, J. He, Z. Zhu, L. Kong, G. Kalimuldina, X. Cheng, Y. Wu, *Energy Mater. Adv.* **2024**, *5*, 0084.
- [33] W. H. Zhang, L. W. Liang, F. Zhao, Y. Liu, L. R. Hou, C. Z. Yuan, *Electrochim. Acta* **2020**, *340*, 10.
- [34] F. Schipper, M. Dixit, D. Kovacheva, M. Talianker, O. Haik, J. Grinblat, E. M. Erickson, C. Ghanty, D. T. Major, B. Markovsky, D. Aurbach, *J. Mater. Chem. A* **2016**, *4*, 16073.
- [35] B. Zhang, C. Zheng, Z. M. Xiao, K. Y. Xian, H. Wen, N. Lu, X. Y. He, L. Ye, J. X. Wang, X. Ou, C. H. Wang, *Appl. Surf. Sci.* **2025**, *684*, 8.
- [36] W. D. Li, H. Y. Asl, Q. Xie, A. Manthiram, *J. Am. Chem. Soc.* **2019**, *141*, 5097.
- [37] W. Liu, P. Oh, X. Liu, M. J. Lee, W. Cho, S. Chae, Y. Kim, J. Cho, *Angew. Chem.-Int. Edit.* **2015**, *54*, 4440.
- [38] J. X. Shen, H. Li, H. Y. Qi, Z. Lin, Z. H. Li, C. B. Zheng, W. T. Du, H. Chen, S. Q. Zhang, *J. Energy Chem.* **2024**, *88*, 428.

- [39] L. S. Ni, H. Y. Chen, J. Q. Gao, Y. Mei, H. J. Wang, F. J. Zhu, J. N. Huang, B. C. Zhang, W. Xu, B. Song, Y. Y. Zhang, W. T. Deng, G. Q. Zou, H. S. Hou, Y. G. Zhou, X. B. Ji, *Nano Energy* **2023**, *115*, 11.
- [40] J. Y. Liao, S. M. Oh, A. Manthiram, *ACS Appl. Mater. Interfaces* **2016**, *8*, 24543.
- [41] T. C. Liu, L. Yu, J. Lu, T. Zhou, X. J. Huang, Z. H. Cai, A. Dai, J. Gim, Y. Ren, X. H. Xiao, M. V. Holt, Y. S. Chu, I. Arslan, J. G. Wen, K. Amine, *Nat. Commun.* **2021**, *12*, 10.
- [42] T. Chen, F. Wang, X. Li, X. X. Yan, H. Wang, B. W. Deng, Z. W. Xie, M. Z. Qu, *Appl. Surf. Sci.* **2019**, *465*, 863.
- [43] Q. M. Gan, N. Qin, Z. Q. Li, S. Gu, K. M. Liao, K. L. Zhang, L. Lu, Z. H. Xu, Z. G. Lu, *Nano Res.* **2023**, *16*, 513.
- [44] Z. H. Cui, P. Zuo, Z. Z. Guo, C. M. Wang, A. Manthiram, *Adv. Mater.* **2024**, *36*, 11.
- [45] L. W. Liang, M. S. Su, Z. F. Sun, L. X. Wang, L. R. Hou, H. D. Liu, Q. B. Zhang, C. Z. Yuan, *Sci. Adv.* **2024**, *10*, 16.
- [46] X. M. Yang, A. L. Rogach, *Adv. Energy Mater.* **2019**, *9*, 10.
- [47] H. P. Yang, H. H. Wu, M. Y. Ge, L. J. Li, Y. F. Yuan, Q. Yao, J. Chen, L. F. Xia, J. M. Zheng, Z. Y. Chen, J. Duan, K. Kisslinger, X. C. Zeng, W. K. Lee, Q. B. Zhang, J. Lu, *Adv. Funct. Mater.* **2019**, *29*, 13.
- [48] M. Chang, F. Y. Cheng, W. Zhang, M. Y. Liao, Q. Li, C. Fang, J. T. Han, *ACS Nano* **2024**, *19*, 712.
- [49] X. M. Fan, G. R. Hu, B. Zhang, X. Ou, J. F. Zhang, W. G. Zhao, H. P. Jia, L. F. Zou, P. Li, Y. Yang, *Nano Energy* **2020**, *70*, 11.
- [50] L. W. Liang, X. Y. Li, M. S. Su, L. X. Wang, J. F. Sun, Y. Liu, L. R. Hou, C. Z. Yuan, *Angew. Chem.-Int. Edit.* **2023**, *62*, 10.
- [51] J. X. Liu, J. Q. Wang, Y. X. Ni, J. D. Liu, Y. D. Zhang, Y. Lu, Z. H. Yan, K. Zhang, Q. Zhao, F. Y. Cheng, J. Chen, *Angew. Chem. Int. Edit.* **2022**, *61*, 9.

---

Manuscript received: March 31, 2025

Revised manuscript received: May 4, 2025

Version of record online:

---